Journal of Applied Fluid Mechanics, Vol. 18, No. 2, pp. 518-534, 2025.
Available online at www.jafmonline.net, ISSN 1735-3572, EISSN 1735-3645.
https://doi.org/10.47176/jafm.18.2.2488

Assessing Energy Loss and Entropy Production in a Centrifugal Pump with Various Impeller Blade Trailing Edges

H. Li[1], Y. Chen[2], L. Bai[3], W. Shi[4] and L. Zhou[3†]

[1] *School of Energy and Power Engineering, Xihua University, Chengdu 610039, China*
[2] *Shanghai Shangyuan Pump Manufacturing Co., Ltd, Shanghai 201508, China*
[3] *National Research Center of Pumps, Jiangsu University, Zhenjiang 212013, China*
[4] *College of Mechanical Engineering, Nantong University, Nantong 226019, China*

†Corresponding Author Email: lingzhou@ujs.edu.cn

ABSTRACT

The centrifugal pump holds significant prominence as a widely adopted power machinery in mechanical industries. This study aims to uncover the influence of blade trailing edges on the energy performance of centrifugal pumps. Sixteen types of blade trailing edge models, including Bezier trailing edges, rounded pressure side, cut suction side, and original blade trailing edges, are examined both numerically and experimentally. Entropy production power and energy loss for each domain with different trailing edge models are computed using entropy production theory and the pressure drop method, respectively. The correlation between them and the interaction of energy loss in various domains are determined through Spearman correlation analysis. Furthermore, the energy loss and efficiency of the centrifugal pump are decomposed and explored. Finally, the impact of different trailing edges on each component of shaft power is analyzed. The study findings indicate that increasing the radius of the trailing edge leads to higher head, while a thinner trailing edge enhances efficiency. Consistent trends are observed in entropy production and energy loss across different blade trailing edges. Modifying the impeller trailing edge significantly affects not only the impeller but also the cavity, diffuser, and outlet chamber, with minimal impact on the inlet chamber. Thinning the blade trailing edge can decrease energy loss and entropy production. Proper design of the blade trailing edge can effectively reduce the pressure pulsation near the impeller outlet in the stator. This study serves as a valuable reference for the design and research of centrifugal pump blade trailing edges.

Article History

Received December 3, 2023
Revised August 26, 2024
Accepted September 1, 2024
Available online December 4, 2024

Keywords:

Bezier curve
Blade trailing edge
Centrifugal pump
Energy loss
Entropy production

1. INTRODUCTION

The centrifugal pump finds extensive application in water circulating systems of thermal power plants, nuclear power stations, pumped-storage power plants, and various other fields, making a significant contribution to the efficient utilization of renewable energy (El-Emam et al., 2022). Serving as the pivotal energy conversion component of the centrifugal pump (Cui et al., 2020a), the impeller facilitates the transfer of mechanical energy to the liquid passing through it by acting upon the liquid via its rotating blades (Huang et al., 2021). The characteristics of the impeller are predominantly determined by the flow pattern at its inlet and outlet, as postulated by Euler's turbine equation. Moreover, the velocity distributed at the impeller outlet profoundly influences the flow within the diffuser. The flow dynamics within the impeller affects more than energy transmission and losses in the impeller, it also affects pressure distribution and flow separation in downstream components (Gülich, 2020).

Modifying the shape of the blade trailing edge (BTE) can alter the flow pattern at the impeller outlet, consequently affecting pump performance. Skillful adjustment of the BTE shape can effectively enhance pump performance. Experimentally altering the pressure side (PS) of the BTE with a fixed angle in a centrifugal pump initially resulted in a decrease in head followed by an increase with increasing cutting volume; however, cutting the suction side (SS) of the BTE led to a consistent increase in head (Kikuyama et al., 1985). Rounding the SS

NOMENCLATURE

H	head	q	leakage flow rate
H_{d}	rated head	$S_{pro,W}$	local entropy production caused by the wall effect
H_{T}	theoretical head	$\dot{S}_{pro,\bar{D}}$	local entropy production rate by direct dissipation
Δh	hydraulic head loss	$\dot{S}_{pro,D'}$	local entropy production rate by indirect dissipation
P	shaft power	ρ_{s}	Spearman correlation coefficient
P_{u}	useful power	η_m	mechanical efficiency
P_{m}	disk friction loss power	η_{v}	volumetric efficiency
P_{v}	volumetric loss power caused by leakage	η_h	hydraulic efficiency
P_{h}	hydraulic loss power	η	pump efficiency
P_{loss}	power loss by pressure drop method	**Subscripts**	
$P_{pro,\bar{D}}$	entropy production power by direct dissipation	in	inlet chamber
$P_{pro,D'}$	entropy production power by indirect dissipation	imp	impeller
$P_{pro,W}$	entropy production power by the wall effect	cav	pump cavity
P_{pro}	total entropy production power	dif	diffuser
Q_{d}	rated flow rate	out	outlet chamber
Q	flow rate		

of the blade trailing edge in a mixed flow pump could enhance head and improve efficiency, particularly at larger flow rates, thus widening the efficiency range (Wu et al., 2015). Cutting the BTE of a centrifugal pump with V-cut, circular, or elliptical profiles on the PS increased head and efficiency compared to the original configuration, while reducing vortex intensity at the BTE. The impact of modifying BTE on sewage pumps with varying specific speeds differed; under-filing the BTE was more effective in increasing pump head and efficiency than default and straight-cut BTE for low blade trailing angles of the camber line (Litfin et al., 2017).

Studies on hydrofoils (Bourgoyne et al., 2005) reveal that the trailing edge's shape significantly influences wake development and vortex shedding (Mosallem, 2008). Thicker or blunter trailing edges intensify vortex shedding, leading to increased pressure pulsations (Do et al., 2010). Beveling the trailing edge can mitigate vibration induced by vortices (Zobeiri et al., 2012). Due to impeller rotation, fluid within the centrifugal pump impeller experiences centrifugal and Coriolis forces (Farge et al., 1992). Consequently, due to Coriolis force and deceleration, fluid near the impeller outlet flows from the SS to the PS, forming a non-uniform secondary flow with a high-velocity jet zone near the PS and a low-velocity wake zone near the SS (Abramian & Howard, 1994).

This non-uniform flow induces pressure pulsations dominated by blade frequency and its harmonic frequencies due to rotor-stator interaction (RSI) (Keller et al., 2014). Modifying the profile of the BTE can alter the pressure-velocity distribution around the impeller outlet, impacting the jet-wake region (Wu et al., 2021a), thereby influencing the unsteady pressure pulsations caused by RSI, which in turn affect fluid-induced vibration and noise (Gao et al., 2016). Numerous researchers have explored the effect of various BTE shapes on the dynamic characteristics of pumps. For example, implementing a V-shaped cut at the BTE of a double-suction pump has been shown to effectively mitigate pressure pulsation and vibration during off-design operational conditions (Al-Qutub et al., 2012). Similarly, adopting elliptical shapes on the suction side and both sides of the BTE has been found to significantly decrease vortex intensity, mitigate pressure pulsation, and enhance pump efficiency (Gao et al., 2016; Zhang et al., 2019). Furthermore, optimizing cutting angles for the trailing edge of straight blades in centrifugal pumps has proven beneficial, positively impacting head, efficiency, and reducing pressure pulsation and vibration displacement (Cui et al., 2020b). Complementary numerical simulations and high-speed camera experiments have demonstrated the superior performance of a round BTE compared to a trimmed BTE, showcasing improved performance for both single-phase and liquid-gas two-phase flows (Mansour et al., 2020). Cutting the PS of the BTE to a lower blade outlet angle could improve pump efficiency and head, decrease velocity in the jet zone near the PS, thus lowering pressure fluctuations (Huang et al., 2021). The utilization of a bionic sinusoidal trailing edge has been found to contribute to reducing energy loss and pressure pulsation in centrifugal pumps (Lin et al., 2021, 2022). Additionally, modifying blade thickness (Qian et al., 2020; Ji et al., 2021;) and blade PS (Wu et al., 2021a, b, 2022) also impacts pump performance and pressure pulsation. Consequently, it is evident that proper design of the BTE holds significant potential in minimizing energy loss, improving the velocity and pressure uniformity around the impeller outlet, and dampening the jet-wake structure,

leading to optimal pump performance, reduced pressure pulsation, and minimized vibration.

Previous research primarily employed ellipses, arcs, or lines to fix the BTE. However, few studies on BTE modified by Bezier curves have been reported. The use of Bezier curves to fix the BTE can ensure that the BTE is tangent to the blade surface with a smooth connection, due to its ability to control the starting and ending directions. Moreover, the Bezier curve simplifies modification of the PS, SS, or both by changing the coordinates of the control points, providing the BTE with continuous curvature.

This paper aims to investigate the effect of BTE on the performance of a centrifugal pump at rated flow rate using Bezier curves, rounded PS, and cut SS to fix the BTE. The performance and energy characteristics of different BTE models are compared via numerical simulation. Subsequently, correlation analysis of energy loss and entropy production power is conducted, followed by decomposition and analysis of energy loss, efficiency, and shaft power. This study reveals the effect of BTEs on the energy characteristics of the centrifugal pump, providing reference and guidance for centrifugal pump BTE design.

2. GEOMETRY MODEL

The present study investigates a single-stage centrifugal pump with a diffuser (Li et al., 2022). The rated flow rate (Q_d) is 14 m^3/h, the rated head (H_d) is 14 m, and the rotating speed is 2850 rpm, resulting in a specific speed (n_s) of 89.6. Both the impeller and diffuser feature two-dimensional blades. To examine the impact of impeller BTE on pump performance, three methods are used to modify the BTE. These methods include employing a 4th order Bezier curve to adjust the trailing edge on both the PS and SS, rounding the trailing edge on the PS with various radii, and cutting the SS at different angles. A full set of 16 models, with the original one, are obtained.

Figure 1(a) illustrates the utilization of a Bezier curve, plotted using Eq. (1) and controlled by five points (P0-P4), as the trailing edge. For further details on the significance of each control point and the parameter configuration of each BTE model, please refer to (Li et al., 2023). Figures 1(b)-(f) depict five classes of BTE models. To facilitate comparison with the original model, several representative Bezier models are presented in Fig. 1(g). Tables 1 and 2 contain parameters for all BTE models.

$$\begin{aligned} \mathrm{B}(t) &= \sum_{i=0}^{4} \binom{4}{i} P_i (1-t)^{4-i} t^i \\ &= (1-t)^4 P_0 + 4t(1-t)^3 P_1 + 6t^2(1-t)^2 P_2 \\ &\quad + 4t^3(1-t)P_3 + t^4 P_4, \quad t \in [0,1] \end{aligned} \tag{1}$$

3.SIMULATION CONFIGURATION

3.1 Computational Domains and Mesh Generation

Figure 2 outlines the composition of the computational domain for the centrifugal pump, encompassing the impeller, diffuser, cavity, inlet chamber and outlet chamber. To address wear ring clearance leakage and disk friction loss, a full flow field simulation is conducted with a unilateral clearance of 0.5 mm at the wear ring. A structural mesh is employed to discretize all computational domains, with Turbogrid used for meshing the impeller and diffuser, and ANSYS ICEM CFD 19R3 utilized for the remaining domains. For the original model at the rated flow rate, the average y^+ value across all walls is 5.7, with an average y^+ value of 11 for the impeller.

Table 2 Parameters of the rounded PS and cut SS at BTE

M	Name	Description
0	Original	Extend to the meridional trailing edge
11	Round_20	R=20mm
12	Round_30	R=30mm
13	Beta2S_40	β_{2s}=40°
14	Beta2S_60	β_{2s}=60°
15	Beta2S_90	β_{2s}=90°

Table 1 Parameters of the Bezier BTE

M	Name	P_{0x}(mm)	P_{1x}(mm)	P_{3x}(mm)	P_{4x}(mm)
1	Bezier6-0-0-0	6	0	0	0
2	Bezier8-0-0-0	8	0	0	0
3	Bezier12-0-0-0	12	0	0	0
4	Bezier20-0-0-0	20	0	0	0
5	Bezier20-0-0-6	20	0	0	6
6	Bezier20-0-0-12	20	0	0	12
7	Bezier20-0-0-20	20	0	0	20
8	Bezier20-6-6-20	20	6	6	20
9	Bezier20-12-12-20	20	12	12	20
10	Bezier20-20-20-20	20	20	20	20

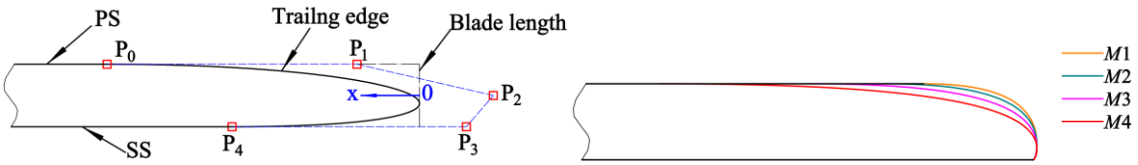

(a) 4th order Bezier curve at the trailing edge (b) Class I

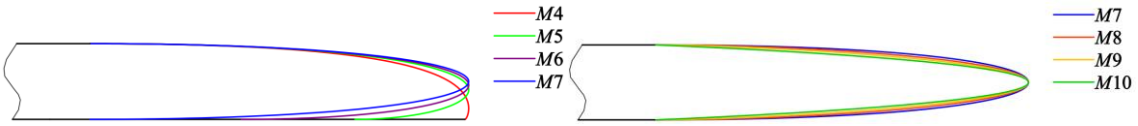

(c) Class II (d) Class III

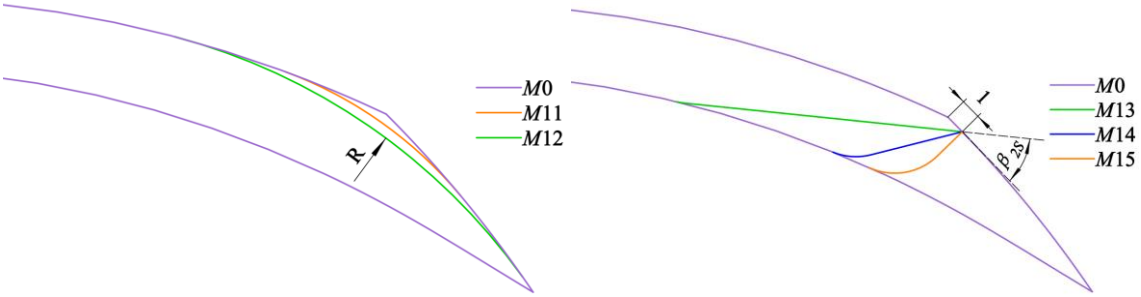

(e) Class IV (f) Class V

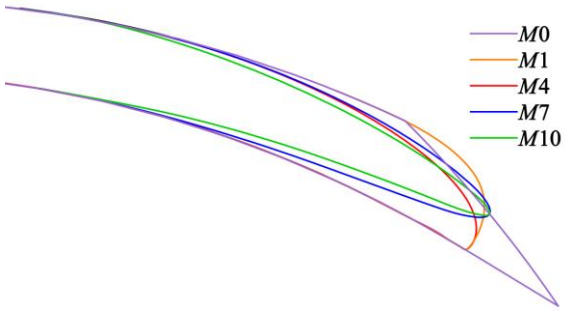

(g) Typical Bezier trailing edges vs. original model

Fig. 1 Different blade trailing edges for investigation

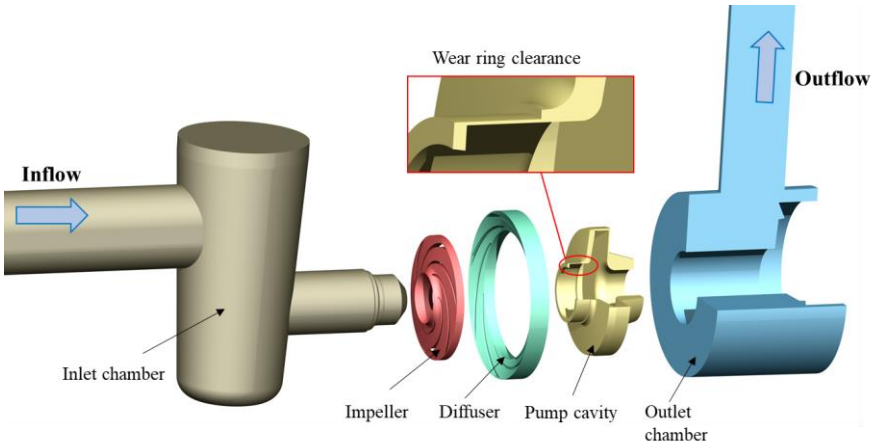

Fig. 2 Computational domain of the centrifugal pump

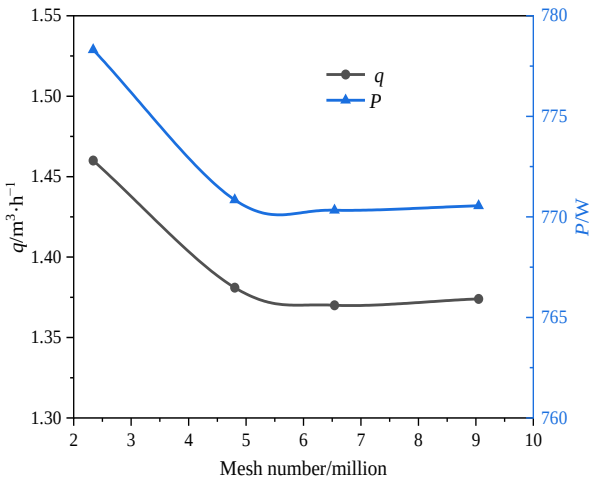

Fig. 3 Mesh sensitivity test

Table 3 Detailed mesh distribution

Domain	Mesh Number
Inlet chamber	695842
Impeller	890136
Pump cavity	907584
Diffuser	1067248
Outlet chamber	1243192
Total	4804002

As shown in Fig. 3, mesh sensitivity testing is conducted using five groups of mesh numbers ranging from 1.27 to 9.05 million. It is observed that pump performance stabilizes as the mesh number increases, with the deviation of leakage flow rate (q) and shaft power (P) being less than 0.51% and 0.04% respectively when the mesh number reaches 4.81 million. Therefore, mesh settings of 4.81 million are chosen for simulating different BTE models. The number of meshes for per domain is presented in Table 3, and the mesh of the centrifugal pump with different BTEs is presented in Fig. 4.

3.2 Boundary Conditions

To evaluate the pump performance and internal flow characteristics, we utilized the commercial CFD software ANSYS-CFX 19R3 to solve the governing equations for the centrifugal pump featuring various BTE models. A mass flow inlet boundary condition was set at the inlet, while at the outlet, an opening outlet boundary condition with a relative pressure of 0 Pa was applied. The impeller was defined as a rotating domain, with the remaining components set as stationary domains. For steady simulations, the frozen rotor was used for data transfer between the rotating and stationary domains. All solid walls were assigned a no-slip wall condition, and wall roughness was neglected. Water at 25°C served as the working medium. The SST k-ω turbulence model, enhanced by automatic wall functions, was chosen to

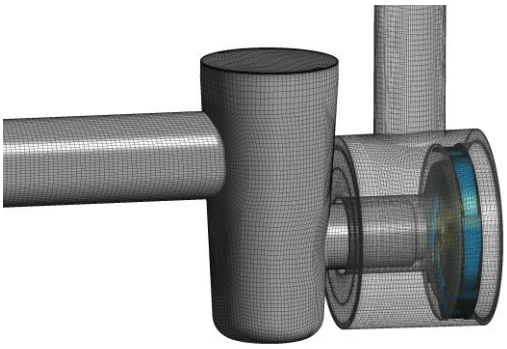

(a) Overall meshes

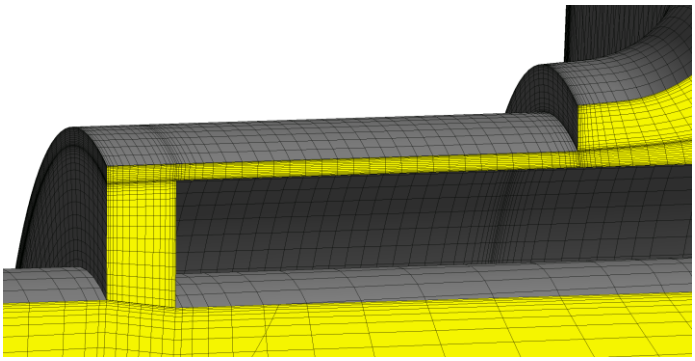

(b) Wear ring clearance

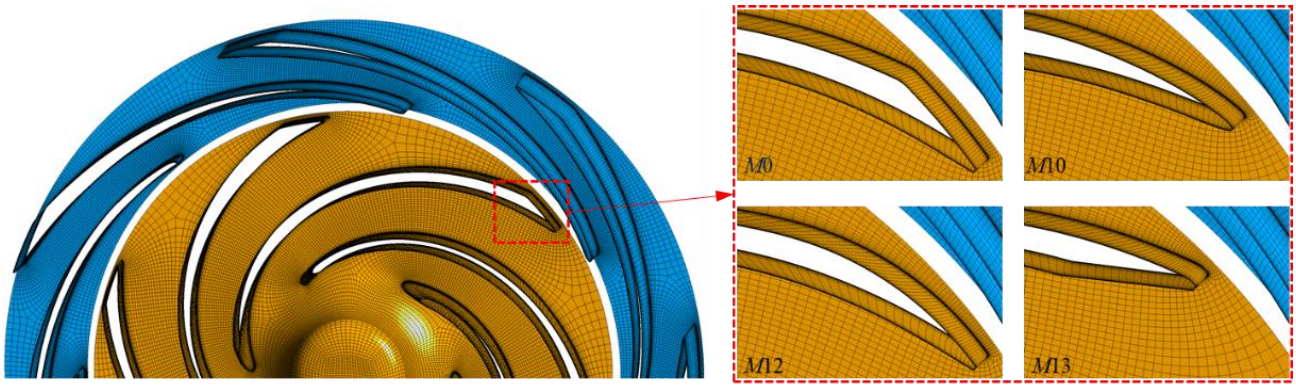

(c) Different BTE

Fig. 4 Meshes of the centrifugal pump and BTE

close the RANS equations due to its accurate prediction capabilities for complex flows featuring flow separation caused by strong adverse pressure gradients (Wang et al., 2019; Han et al., 2021). A high-resolution scheme was employed to solve the convection term, with a convergence criterion for the root-mean-square residuals set to 10^{-5}(Zhao et al., 2024). For unsteady simulations, the Transient Rotor Stator method is employed for data transfer between the rotating and stationary domains. The time step is set at 5.84795×10^{-5} s, which corresponds to the time taken for the impeller to rotate by 1°. The total duration is configured as 0.315789 s, equivalent to the time for 15 revolutions of impeller.

4. ENTROPY PRODUCTION THEORY

Viscosity within the medium leads to a fraction of the fluid's kinetic and pressure energies being inevitably converted into internal energy by shear forces in the near-wall region of turbulent flows (Kock & Herwig, 2004). Unstable turbulent pulsations result in energy losses irreversibly transformed into internal energy (Li et al., 2017). These energy losses contribute to an increase in entropy. Hence, the entropy production method is beneficial for assessing energy losses in centrifugal pumps with different trailing edges (Kock & Herwig, 2005; Ji et al., 2020; Zhou et al., 2022). Given water's high specific heat capacity as the working fluid in centrifugal pumps, the resulting temperature rise from energy dissipation is minimal, enabling it to be treated as a constant temperature. Assuming a temperature of T = 298.15 K and disregarding heat transfer and temperature rise, local entropy production can be computed using the following approach:

$$\dot{S}_{pro,D}=\dot{S}_{pro,\overline{D}}+\dot{S}_{pro,D'} \tag{2}$$

$$\dot{S}_{pro,\overline{D}}=\frac{\mu}{\overline{T}}\left\{2\left[\left(\frac{\partial\overline{u_1}}{\partial x_1}\right)^2+\left(\frac{\partial\overline{u_2}}{\partial x_2}\right)^2+\left(\frac{\partial\overline{u_3}}{\partial x_3}\right)^2\right]+\left(\frac{\partial\overline{u_2}}{\partial x_1}+\frac{\partial\overline{u_1}}{\partial x_2}\right)^2+\left(\frac{\partial\overline{u_3}}{\partial x_1}+\frac{\partial\overline{u_1}}{\partial x_3}\right)^2+\left(\frac{\partial\overline{u_2}}{\partial x_3}+\frac{\partial\overline{u_3}}{\partial x_2}\right)^2\right\} \tag{3}$$

$$\dot{S}_{pro,D'}=\frac{\mu}{\overline{T}}\left\{2\left[\overline{\left(\frac{\partial u_1'}{\partial x_1}\right)^2}+\overline{\left(\frac{\partial u_2'}{\partial x_2}\right)^2}+\overline{\left(\frac{\partial u_3'}{\partial x_3}\right)^2}\right]+\overline{\left(\frac{\partial u_2'}{\partial x_1}+\frac{\partial u_1'}{\partial x_2}\right)^2}+\overline{\left(\frac{\partial u_3'}{\partial x_1}+\frac{\partial u_1'}{\partial x_3}\right)^2}+\overline{\left(\frac{\partial u_2'}{\partial x_3}+\frac{\partial u_3'}{\partial x_2}\right)^2}\right\} \tag{4}$$

where $\dot{S}_{pro,\overline{D}}$ is entropy production rate by direct dissipation, $\dot{S}_{pro,D'}$ is entropy production rate by indirect dissipation.

In the SST k-ω turbulence model, $\dot{S}_{pro,D'}$ can be approximated as (Herwig & Kock, 2006; Ji et al., 2020):

$$\dot{S}_{pro,D'}=\beta\frac{\rho\omega k}{T} \tag{5}$$

where β = 0.09，ω is turbulent eddy frequency (s^{-1}), k is turbulent energy (m^2/s^2).

The entropy production power also accounts for the local entropy production induced by the wall effect (Li et al., 2017).

$$S_{pro,W}=\frac{\vec{\tau}\cdot\vec{v}}{T} \tag{6}$$

where，$\vec{\tau}$ is the wall shear stress (Pa)，$\vec{v}$ is the velocity near the wall (m/s).

By integrating the local entropy production rate over the volume and surfaces of the computational domain and multiplying by T, the components of entropy production power (W) on the domain can be obtained:

$$P_{pro,\overline{D}}=T\int_V\dot{S}_{pro,\overline{D}}dV \tag{7}$$

$$P_{pro,D'}=T\int_V\dot{S}_{pro,D'}dV \tag{8}$$

$$P_{pro,W}=T\int_A S_{pro,W}dA \tag{9}$$

The entropy production power of a domain is calculated as follows:

$$P_{pro}=P_{pro,\overline{D}}+P_{pro,D'}+P_{pro,W} \tag{10}$$

5. RESULTS AND DISCUSSION

5.1 Experimental Setup and Validation

The centrifugal pump experiment was carried out using a closed pump test rig, as depicted in Fig. 5. A variable frequency motor was employed to drive the pump, and the flow rate was measured through an electromagnetic flowmeter featuring a range of 3.5-35 m^3/h and an accuracy of ±0.5%. Inlet and outlet pressures of the centrifugal pump were monitored by corresponding pressure sensors, with a range of -100 to 100 KPa and 0 to 1 MPa, respectively, offering an accuracy of ±0.075%. Throughout the experiment, the inlet valve remained fully open, allowing the pump's flow rate to be regulated through the outlet valve. Figure 6 presents a comparative analysis of the simulated and experimental results of $M0$, revealing a consistent trend, with the head being closest around 10 m^3/h. With an increase in flow rate, the deviation in head also exhibits an upward trend, reaching a relative error of 7.6% at the rated flow rate of 14 m^3/h. However, the deviation in efficiency at the rated point is smaller, with a relative error of 1.5% at the rated flow rate. The experimental verification results provide sufficient evidence to support the credibility of the simulation results.

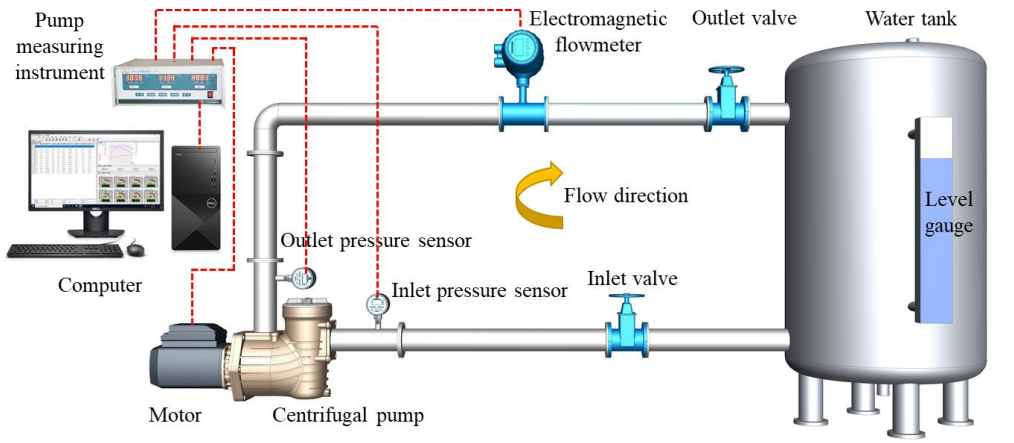

Fig. 5 Schematic diagram of the test rig

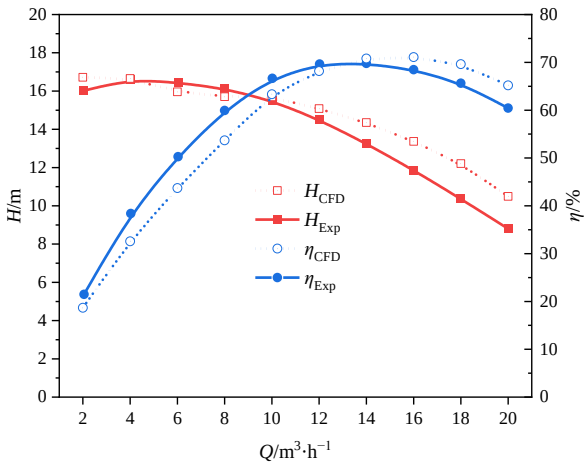

Fig. 6 Comparison of head and efficiency between experimental and numerical results of *M*0

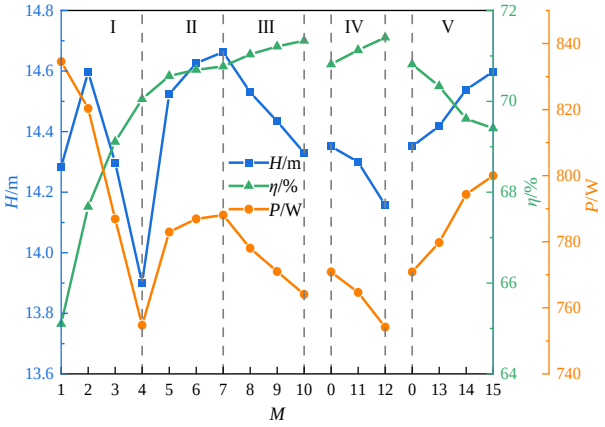

Fig. 7 Performance comparison of different BTE models

5.2 Effect of BTE on the Performance of Rated Flow Rate

Figure 7 presents the simulated performance of various BTE models at the rated flow rate. In Class I, from *M*1 to *M*4, the radius of the BTE on PS gradually decreases, while the radius on the SS remains constant, resulting in a thinner BTE and an increase in efficiency. The power also decreases gradually, and the head exhibits a decreasing trend due to the reduction in the BTE radius. However, an exception exists where the head of *M*1 is lower than that of *M*2. This can be attributed to the head being determined by the difference between theoretical head and hydraulic loss. Since *M*1 has the thickest trailing edge, the hydraulic loss caused by strong wake vortex outweighs the theoretical head increase resulting from the larger trailing edge radius, leading to a lower head compared to *M*2. In Class II, from *M*4 to *M*7, the radius of the trailing edge on both sides gradually increases, but the radius of the SS increases more than that of the PS, leading to a gradually thinner trailing edge. Head, power, and efficiency all increase gradually, with the largest performance increment observed from *M*4 to *M*5 due to the largest increase in BTE radius. In Class III, from *M*7 to *M*10, the radius of the BTE on PS decreases gradually, while the radius of the BTE on SS increases gradually, resulting in a thinner BTE symmetrically with the meanline as the center. The head and power gradually decrease, while the efficiency gradually increases due to the thinner BTE. From *M*1 to *M*10, it is evident that thinning the BTE can increase the efficiency of the centrifugal pump. In Class IV, the head and power gradually decrease and the efficiency gradually increases as the round radius on the PS increases. In Class V, as the cutting angle on the SS increases, the head and power show a gradual increase, but efficiency gradually decreases due to the blunter BTE. It is demonstrated that the BTE has a profound impact on pump performance.

5.3 Analysis of Energy Loss and Entropy Production Power for Different BTE Models

To conduct a quantitative analysis of energy losses in each component of the pump, the pressure drop method is employed, considering each computational domain as a control volume. Energy loss can be calculated using the following equation:

$$P_{loss} = T\omega - \iint_A p_t \boldsymbol{v}.\boldsymbol{n} dA \tag{11}$$

Here, T represents the torque, ω denotes the rotational speed, the first right term represents the power acting on the control volume, A represents the outside surface of the

control volume, p_t represents the total pressure, $\boldsymbol{n}$ represents the direction normal to the outer surface of the control volume, and the second term on the right side represents the increment of useful energy within the control volume.

Figure 8(a) illustrates the energy loss of each domain at the rated flow rate of different BTE models. In Class I, with the increase of P_{1x}, the BTE becomes thinner, and the energy loss of the impeller, cavity, diffuser, and outlet chamber decreases significantly, while the energy loss of the inlet chamber remains almost unchanged. In Class II, as P_{4x} increases, the BTE becomes thinner, and the energy loss of the impeller gradually decreases, while the energy loss of the remaining domains increases slightly. This increase may be due to the increase in radius and blade angle at SS of the BTE, resulting in higher velocity at the impeller outlet and an increase in impact loss and friction loss of the diffuser. In Class III, the simultaneous increase in P_{1x} and P_{3x} results in a gradual thinning of the BTE and a decrease in energy loss in each domain. In Class IV, as the rounding radius on the PS of the BTE increases, the energy loss decreases in the impeller, cavity, and diffuser, while it slightly increases in the outlet chamber. In Class V, the rise in the cutting angle on the suction side of the BTE corresponds to an augmented bluntness of the BTE profile, consequently resulting in escalated energy loss within each domain. From the observations above, it is evident that the modified BTE in Class I has the greatest impact on energy loss. The different BTE models significantly affect the energy loss in the impeller, cavity, diffuser, and outlet chamber, but have little effect on the inlet chamber. Among all the domains, the cavity exhibits the highest energy loss, followed by the impeller, diffuser, and outlet chamber, while the inlet chamber experiences the least energy loss.

Figure 8(b) depicts the total entropy production power of individual domains for various BTE models at the rated flow rate. Comparing Fig. 8(a) and Fig. 8(b), it is evident that the influence of different BTE on energy loss and entropy production power is remarkably consistent, indicating the validity of analyzing energy loss in the centrifugal pump with entropy production theory (Li et al., 2017; Zhang et al., 2020). However, it is worth emphasizing that the entropy production power is slightly smaller than the energy loss power calculated using the pressure drop method. Moreover, there is little discrepancy between the entropy production power of the diffuser and the impeller. In fact, in most BTE models, the entropy production power of the diffuser even exceeds that of the impeller, which contrasts the findings of the energy loss analysis.

Based on the analysis above, the impeller exhibits the highest energy loss among all the domains, except for the cavity, which will be discussed in section 5.5. The energy loss in the diffuser is comparatively lower than that in the impeller, while the entropy production power in the diffuser closely resembles that of the impeller. Additionally, the impeller is the only part of the centrifugal pump that is modified and is responsible for the differences in performance among each BTE model.

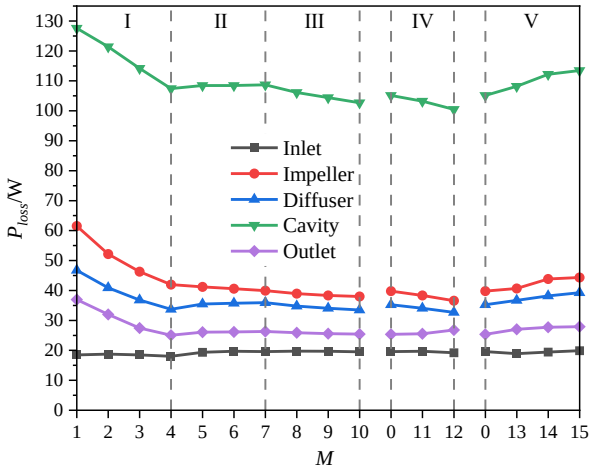

(a) Energy loss power

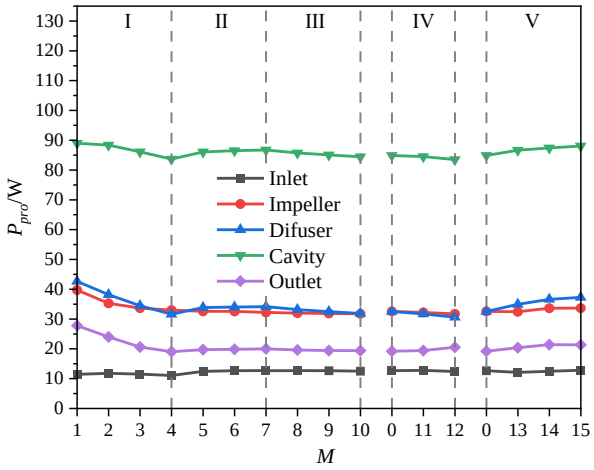

(b) Entropy production power

Fig. 8 Energy loss and entropy production power of each domain for different BTE models

The diffuser plays a crucial role in converting the kinetic energy of the impeller outflow into pressure energy, thereby significantly impacting performance (Gülich, 2020). Figure 9(a) and Fig. 9(b) compare the energy loss and entropy power production components of the impeller and diffuser at the rated flow rate for various BTE models, respectively. As seen in Fig. 9(a), the variation trend of P_{pro} and P_{loss} in the impeller is consistent, and the influence of different BTE on P_{loss} is more significant than that of P_{pro}, leading to a larger deviation between P_{loss} and P_{pro} in models with large energy loss and smaller deviation in models with small energy loss. The model with the largest deviation is $M1$ with a deviation of 35.3%, while the model with the smallest deviation is $M12$ with a deviation of 13.2%. The average deviation of all models is 21.4%. Among the entropy production power components in the impeller, the wall entropy production power $P_{pro,W}$ caused by friction is the largest, followed by the indirect dissipation entropy production power $P_{pro,D'}$ caused by turbulent dissipation, and $P_{pro,\bar{D}}$ caused by the time-averaged velocity gradient is the smallest. Various BTE models exhibit the most pronounced impact on $P_{pro,D'}$, followed by the effect on $P_{pro,W}$, and the least effect on $P_{pro,\bar{D}}$. In Fig. 9(b), the trend of P_{pro} and P_{loss} in the diffuser

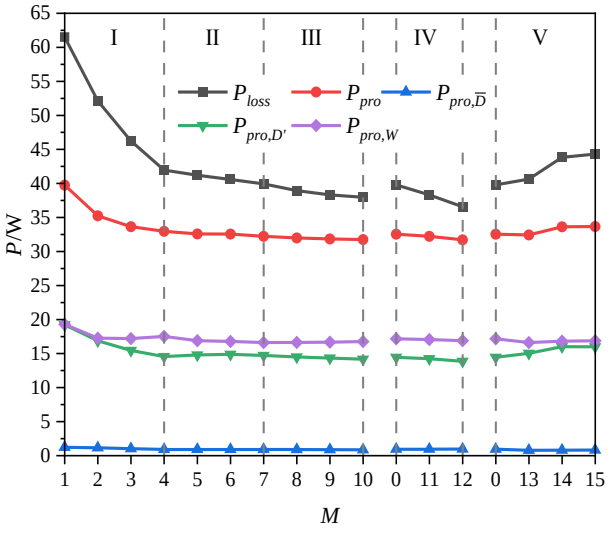

(a) Impeller loss power

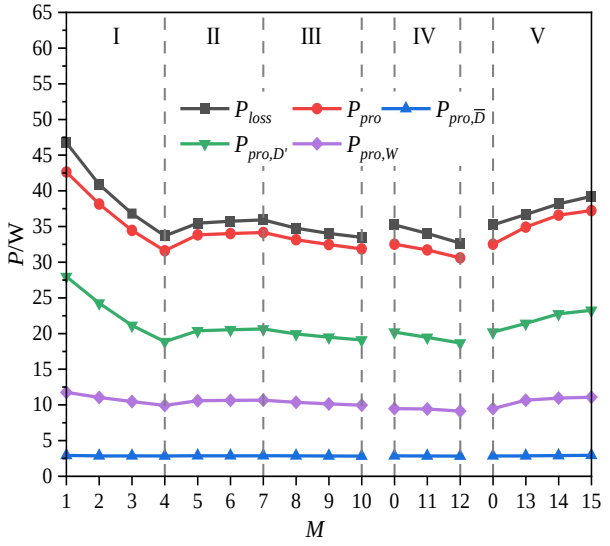

(b) Diffuser loss power

Fig. 9 Energy loss and entropy production power components of impeller and diffuser for different BTE models

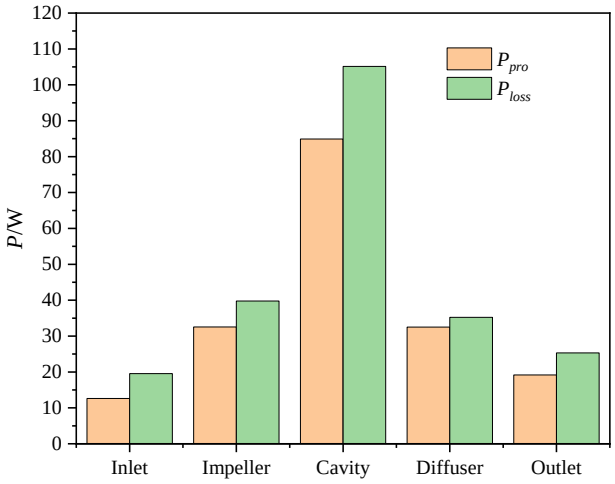

(a) Comparison of energy loss and entropy production power

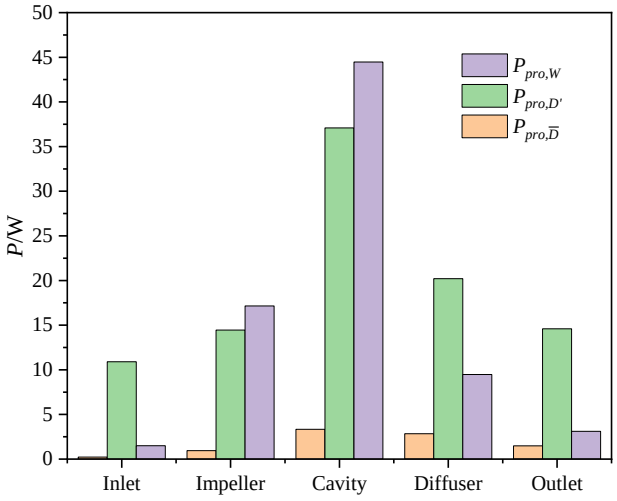

(b) Entropy production distribution

Fig. 10 Energy loss and entropy production power components of each domain for *M*0

is more consistent compared to that of the impeller, resulting in smaller deviation between P_{loss} and P_{pro}. *M*1 still exhibits the largest deviation, reaching 8.7%, and the average deviation of all model schemes is 5.7%. Among the entropy production power components in the diffuser, $P_{pro,D'}$ is the largest, followed by $P_{pro,W}$, which is contrary to the impeller, and $P_{pro,\bar{D}}$ remains the smallest. In comparison, $P_{pro,D'}$, $P_{pro,\bar{D}}$,and $P_{pro,W}$ of the diffuser in different BTE models are 2.4-3.6, 1.29-1.45, and 0.54-0.65 times that of the impeller, respectively.

Due to similarities with other BTE models, *M*0 is taken as an illustrative case to analyze the energy loss and entropy production power among the domains. Fig. 10 illustrates the energy loss and entropy production power of each domain for *M*0. As evident in Fig. 10(a), the trend of energy loss and entropy production power in different domains is consistent, with the energy loss of all domains being larger than the entropy production power. The deviation between energy loss power and entropy production power is the smallest in the diffuser and the largest in the cavity. Figure 10(b) shows the components of the entropy production power in each domain for *M*0, showing that the direct dissipation entropy production power $P_{pro,\bar{D}}$ is the smallest in all domains. The wall entropy production power $P_{pro,W}$ is the largest in the cavity and impeller, while it is smaller than $P_{pro,D'}$ to become the second largest in the rest of the domains, decreasing in the order of cavity, impeller, diffuser, outlet chamber, and inlet chamber. This hierarchy is due to $P_{pro,W}$ being obtained by integrating the product of the shear stress and the velocity near the wall.

The average relative velocity on the first layer of the grid of different domains in *M*0 is presented in Table 4. Due to the presence of the outer cover of the impeller, rotating at the same speed as the impeller, the average velocity near the wall of the cavity is the highest. Following that, the impeller exhibits the second-highest velocity, attributed to the centrifugal force and Coriolis force induced by its rotation. As for the diffuser, it decelerates the high-speed outflow from the impeller,

Table 4 Average relative velocity on the first grid layer of different domains for *M*0

Domain	Inlet	Impeller	Cavity	Diffuser	Outlet
v (m/s)	0.24	3.91	6.69	1.51	0.49

converting kinetic energy into pressure energy before flowing into the outlet chamber, resulting in a lower average velocity compared to the impeller but higher than that of the outlet chamber. Despite the outlet angle of the diffuser not being 90 degrees, there remains a certain amount of velocity circulation in the flow into the outlet chamber, causing a higher average velocity compared to the inlet chamber, which has the smallest average velocity.

5.4 Spearman Correlation Analysis of Energy Loss and Entropy Production Power

Similar trends observed in the energy loss and entropy production power of different BTE models can be identified. To quantify the correlation between energy loss and entropy production power across different domains, as well as the relationship of energy loss within various domains, a Spearman correlation analysis method is employed. Consider two random variables, X and Y, each with a total of N observations. The i^{th} variable of X and Y can be represented as x_i and y_i, respectively. Additionally, x_i' and y_i' represent the rankings assigned to x_i and y_i, respectively. The Spearman correlation coefficient, ρ_s, between X and Y can be obtained using Eq. (12) (Meng et al., 2019). ρ_s falls within the range of [-1, 1]. A correlation value of 0 indicates the absence of any correlation, while a value falling within the interval of [-1, 0) signifies a negative correlation, and a value within the range of (0, 1] implies a positive correlation.

$$\rho_s = \frac{\sum_{i=1}^{N}\left(x_i' - \overline{x'}\right)\left(y_i' - \overline{y'}\right)}{\sqrt{\sum_{i=1}^{N}\left(x_i' - \overline{x'}\right)^2 \sum_{i=1}^{N}\left(y_i' - \overline{y'}\right)^2}} \tag{12}$$

Given that 16 BTE models are calculated in this study, N = 16. Figure 11(a) shows the Spearman correlation coefficients of energy loss and entropy production power among different domains. Overall, there is an extremely strong positive correlation with correlation coefficients above 0.9 between energy loss and entropy production power of each domain. The highest correlation coefficient is 0.99 for the diffuser and outlet chamber, followed by 0.96 for the impeller and inlet chamber, with the lowest coefficient at 0.9 for the cavity. Figure 11(b) shows the correlation of energy loss among each domain. The inlet chamber exhibits a negative correlation with other domains, with a correlation coefficient of only -0.46 with the impeller, and even weaker correlation with other domains. The impeller shows the highest correlation with the cavity at 0.94, followed by the diffuser and outlet chamber, with the weakest correlation observed with the inlet chamber. Similarly, the cavity displays the highest correlation with the impeller and diffuser, both at 0.94, followed by the outlet chamber, with the weakest correlation again with the inlet chamber. The diffuser demonstrates the highest correlation with the cavity, followed by the impeller, the outlet chamber, and the weakest correlation with the inlet chamber. Lastly, the

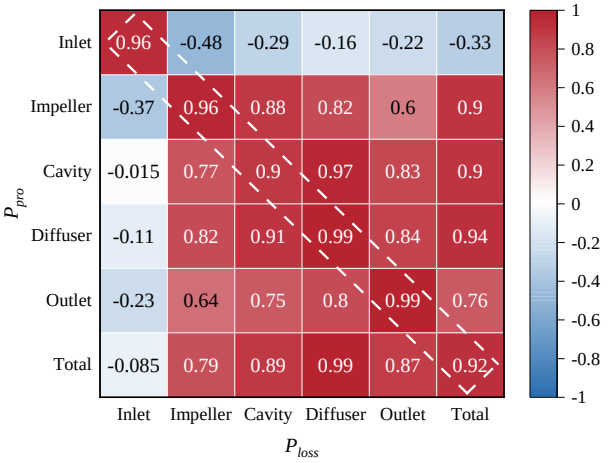

(a) Spearman correlation coefficient between energy loss and entropy production power

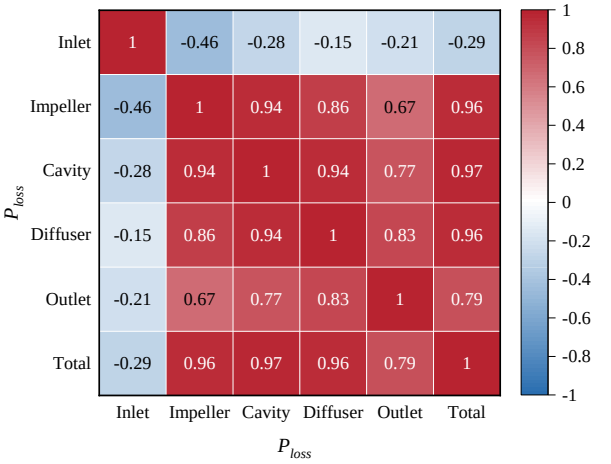

(b) Spearman correlation coefficient of energy loss among different domains

Fig. 11 Correlation analysis of energy loss and entropy

outlet chamber exhibits the highest correlation with the diffuser at 0.83, followed by the cavity and impeller, with the weakest correlation with the inlet chamber. In conclusion, each domain exhibits the highest correlation with its adjacent domains in space, with correlations decreasing as distance increases. The modification of BTE significantly affects the impeller and downstream domains (i.e., the cavity, diffuser, and outlet chamber), but has minimal impact on the upstream inlet chamber.

5.5 Decomposition of Energy Loss for Different BTE Models

Upon reviewing the previous data, it is clear that the cavity experiences the highest losses in both energy loss power and entropy production power. This phenomenon stems from two main factors: disk friction loss due to the

impeller's outer cover rotation, and volumetric loss resulting from leakage through the wear ring. Therefore, we will proceed with the decomposition of energy loss.

The pump's shaft power can be expressed as follows:

$$P = \sum P_{loss} + P_u = P_m + P_v + P_h + P_u \tag{13}$$

$$P_u = \rho g Q H \tag{14}$$

$$\begin{aligned} P_v &= \rho g q H_T \\ &= \rho g q(\Delta h_{q,imp} + \Delta h_{q,cav} + \Delta h_{q,in}) \\ &= P_{v,imp} + P_{v,cav} + P_{v,in} \end{aligned} \tag{15}$$

$$\begin{aligned} P_h &= \rho g Q(H_T - H) \\ &= \rho g Q(\Delta h_{Q,in} + \Delta h_{Q,imp} + \Delta h_{Q,cav} \\ &\quad + \Delta h_{Q,dif} + \Delta h_{Q,out}) \\ &= P_{h,in} + P_{h,imp} + P_{h,cav} + P_{h,dif} + P_{h,out} \end{aligned} \tag{16}$$

$$\begin{aligned} \sum P_{loss} &= P_{loss,in} + P_{loss,imp} + P_{loss,cav} \\ &\quad + P_{loss,dif} + P_{loss,out} \end{aligned} \tag{17}$$

where P is the shaft power (W), P_u is the useful power (W), P_m is the disk friction loss power (W) (without considering the loss of bearing and mechanical seal), P_v is the volumetric loss power caused by leakage (W), P_h is the hydraulic loss power (W), H_T is the theoretical head (m), H is the head (m), and q is the leakage flow rate (m^3/h). $\Delta h_{q,imp}$, $\Delta h_{q,cav}$, $\Delta h_{q,in}$ are the hydraulic head losses (m) of the leakage flow in the impeller, cavity, and inlet chamber, respectively.$\Delta h_{Q,in}$,$\Delta h_{Q,imp}$,$\Delta h_{Q,cav}$,$\Delta h_{Q,dif}$, $\Delta h_{Q,out}$ are the hydraulic head losses (m) of the primary flow in the inlet chamber, impeller, cavity, diffuser, and outlet chamber, respectively.

As illustrated in Fig. 12, it is evident that the leakage flow's direction aligns with that of the primary flow within the impeller. Consequently, the following equation can be derived:

$$\Delta h_{q,imp} = \Delta h_{Q,imp} \tag{18}$$

Replacing Eq. (13) with Eqs. (15)-(18) and sorting them by each domain, the energy loss in each domain is obtained as follows：

$$P_{loss,in} = \rho g q \Delta h_{q,in} + \rho g Q \Delta h_{Q,in} = P_{v,in} + P_{h,in} \tag{19}$$

$$P_{loss,imp} = \rho g (Q+q) \Delta h_{Q,imp} = P_{v,imp} + P_{h,imp} \tag{20}$$

$$\begin{aligned} P_{loss,cav} &= P_m + \rho g q \Delta h_{q,cav} + \rho g Q \Delta h_{Q,cav} \\ &= P_m + P_{v,cav} + P_{h,cav} \end{aligned} \tag{21}$$

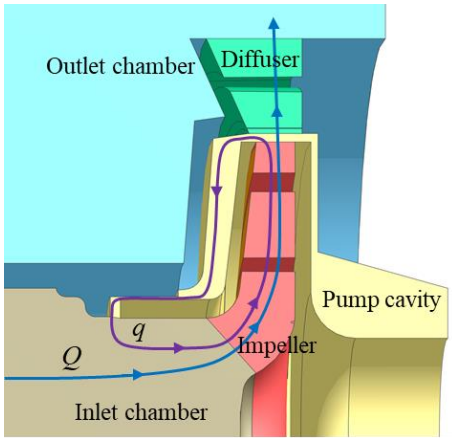

Fig. 12 Schematic diagram of flow direction of primary flow and leakage flow

$$P_{loss,dif} = \rho g Q \Delta h_{Q,dif} = P_{h,dif} \tag{22}$$

$$P_{loss,out} = \rho g Q \Delta h_{Q,out} = P_{h,out} \tag{23}$$

The pump's efficiency components are calculated by Eqs. (24)-(26), and the total efficiency of the pump is calculated by Eq. (27), where η_m denotes the mechanical efficiency, η_v denotes the volumetric efficiency, η_h denotes the hydraulic efficiency, and η denotes the overall pump efficiency.

$$\eta_m = \frac{P - P_m}{P} \tag{24}$$

$$\eta_v = \frac{Q}{Q+q} \tag{25}$$

$$\eta_h = \frac{H}{H_T} \tag{26}$$

$$\eta = \frac{\rho g Q H}{P} = \eta_m \eta_v \eta_h \tag{27}$$

Eq. (21) reveals that the cavity's energy loss comprises three parts: the hydraulic loss of primary flow in the cavity $P_{h,cav}$, the volumetric loss due to leakage $P_{v,cav}$, and the disk friction loss P_m. Figure 13 illustrates the energy loss components of the cavity in different BTE models. $P_{v,cav}$ is the highest, P_m is slightly lower than $P_{v,cav}$, and $P_{h,cav}$ is the lowest. Different BTE models primarily affect $P_{h,cav}$, followed by $P_{v,cav}$, and have the least effect on P_m. Compared with Fig. 7, it is apparent that $P_{v,cav}$ is mainly influenced by head variation. A higher head results in a larger $P_{v,cav}$, aligning consistently with the head. This occurrence stems from the fact that the leakage flow q is governed by the pressure difference between the two ends of the wear ring, which correlates with the head. In Classes I, II, and III, $P_{h,cav}$ declines progressively as the BTE thickness decreases; in Class IV, $P_{h,cav}$ gradually decreases as the round radius on the PS of BTE increases; in Class V, $P_{h,cav}$ increases gradually as the cutting angle on the SS of BTE increases.

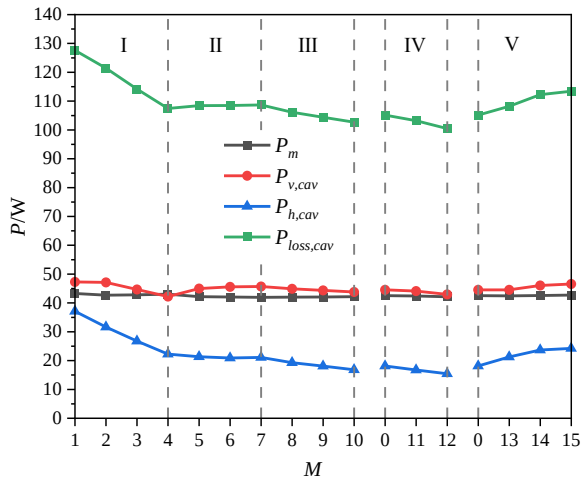

Fig. 13 Components of energy loss in cavity of different BTE models

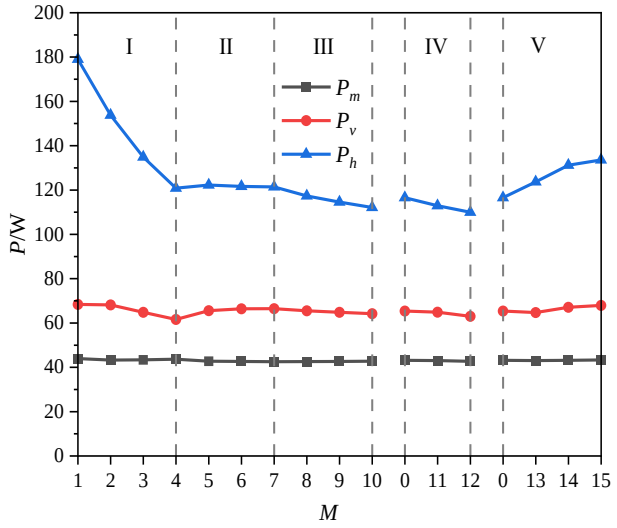

(a) Different components of energy loss

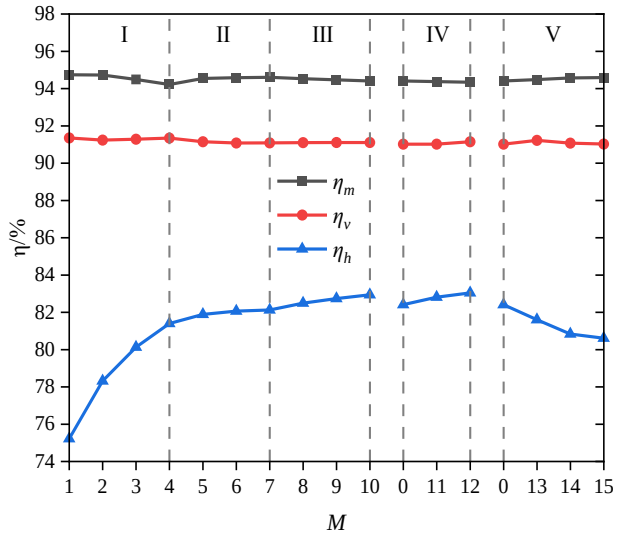

(b) Different components of efficiency

Fig. 14 Energy loss and efficiency of the pump for different BTE models

The energy loss within the pump typically comprises three components (Wang et al., 2017): disc friction loss P_m , volumetric loss P_v (Eq. 15), and hydraulic loss P_h (Eq. 16). Figure 14(a) illustrates each of these components for different BTE models. It is evident that the disc friction loss P_m is the smallest and shows minimal variation across different BTE models. On the other hand, the volumetric loss P_v exceeds P_m, with values ranging from approximately 1.41 to 1.57 times that of P_m for different BTE models, while still maintaining a consistent trend with the head. As for the hydraulic loss P_h, it emerges as the largest contributing factor. Different BTE models have the most substantial impact on P_h, followed by P_v, while P_m remains relatively unchanged. In Classes I, II, and III, P_h gradually decreases as the BTE thickness diminishes. In Class IV, P_h gradually decreases with the increase of the round radius on the PS of BTE. Conversely, in Class V, P_h gradually increases with an increase of the cutting angle on the SS of BTE. Figure 14(b) shows the efficiency components in the pump for different BTE models. Notably, the mechanical efficiency η_m is the highest, followed by the volumetric efficiency η_v, with minimal influence exerted by different BTE models. The hydraulic efficiency η_h records the lowest value and experiences the most significant impact from different BTE models. Therefore, the hydraulic efficiency η_h plays a decisive role in the total efficiency η. This explains why non-full flow field simulation without considering leakage and the outer cover of the impeller can also be used to predict pump performance to some extent. In Classes I, II, and III, η_h gradually increases with a decrease in BTE thickness. In Class IV, η_h gradually increases with an increase in the round radius on the PS of BTE, while in Class V, η_h gradually decreases with an increase in the cutting angle on the SS of BTE.

5.6 Effect of Various BTE on Shaft Power and its Components

The shaft power of the pump is derived from the torque applied to the rotating surfaces, as shown in Fig. 15. The rotating surfaces of the impeller can be divided into five parts: Blades, Shroud on the inner surface of the impeller (Shroud_i), Hub on the inner surface of the

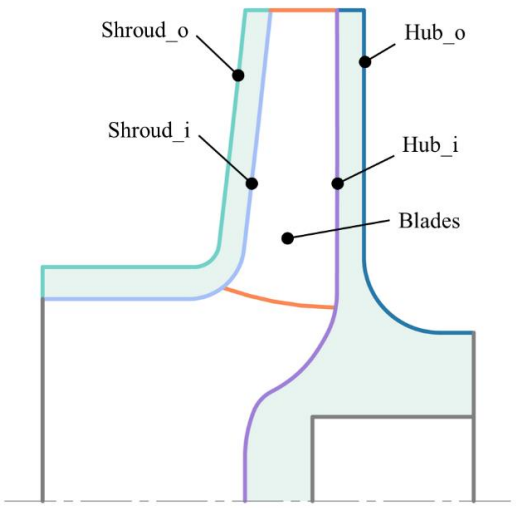

Fig. 15 Surfaces forming the shaft power in meridional section

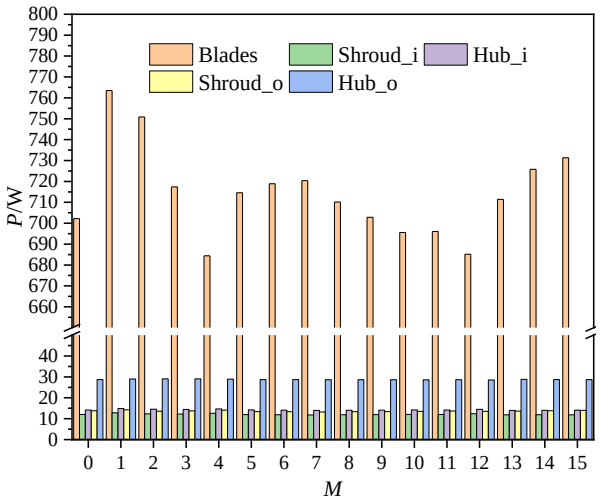

(a) Shaft power of different surfaces for different BTE models

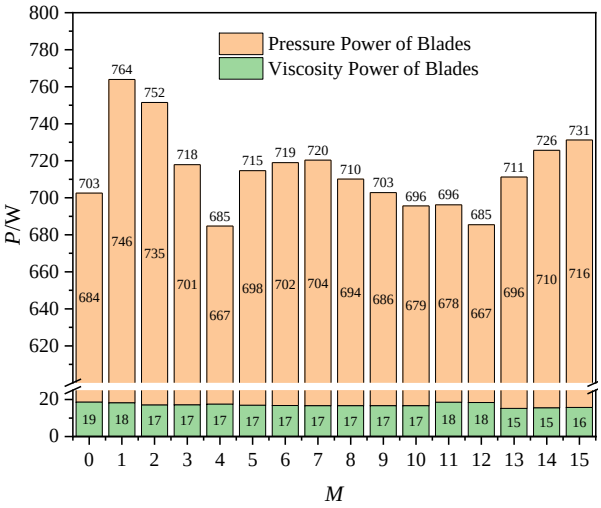

(b) Pressure and viscosity components of blades shaft power for different BTE models

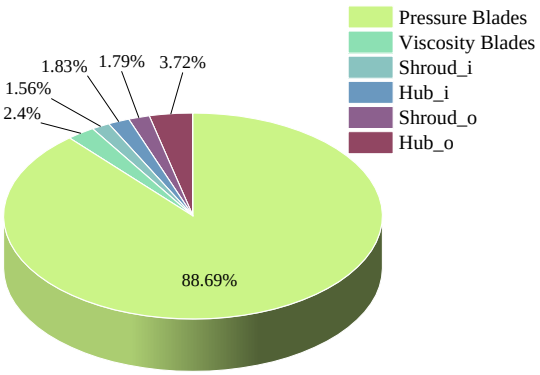

(c) Percentage of shaft power components for *M*0

Fig. 16 Components of shaft power

impeller (Hub_i), Shroud on the outer surface of the impeller (Shroud_o), Hub on the outer surface of the impeller (Hub_o). Figure 16(a) presents the shaft power of different parts for various BTE models. It is evident that the shaft power of the blades is much larger than others, with the shaft power ranking in descending order: Blades > Hub_o > Hub_i > Shroud_o > Shroud_i. With the change of BTE, the power of the blades changes the most, while the other parts change little. Different BTE models have the greatest effect on the power of the blades but little effect on the others. It is well-known that the shaft power of the blades is caused by viscous and static pressure. To examine the impact of various BTE models on these two parts, Fig. 16(b) shows the shaft power generated by viscosity and static pressure on the blades for different BTE models. With the change of BTE, the shaft power caused by pressure varies greatly, while the shaft power caused by viscosity varies little. Taking *M*0 as an example, Fig. 16(c) illustrates the percentages of shaft power of each part, where the shaft power caused by static pressure accounts for the majority, reaching 88.69%. Therefore, the influence of different BTE on the shaft power mainly manifests in the blade load caused by the static pressure.

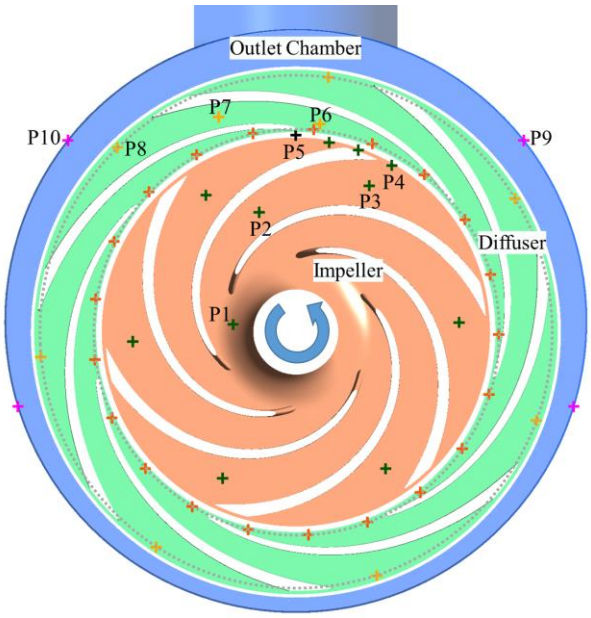

Fig. 17 Distribution of pressure monitoring points in the centrifugal pump

5.7 Effect of Different BTE on Pressure Pulsations

To investigate the impact of different blade trailing edges on the pressure pulsation characteristics of the centrifugal pump, several monitoring points are placed at the intermediate section (Span=0.5) between the impeller and the diffuser, as shown in Fig. 17. Points P1-P4 are located within the impeller, P5 is positioned in the pump cavity between the impeller and diffuser, P6-P8 are within the diffuser, and P9 and P10 are in the outlet chamber. Representative schemes *M*0, *M*10, and *M*12 are selected for unsteady simulation.

$$C_p = \frac{p - \bar{p}}{0.5\rho u_2^2} \tag{28}$$

$$C_p^{p-p} = C_{p,\max} - C_{p,\min} \tag{29}$$

In Fig. 18, the pressure coefficient C_p (Eq. 28) at monitoring points for *M*0, *M*10, and *M*12 at rated flow rate over one revolution is illustrated, along with the peak-to-

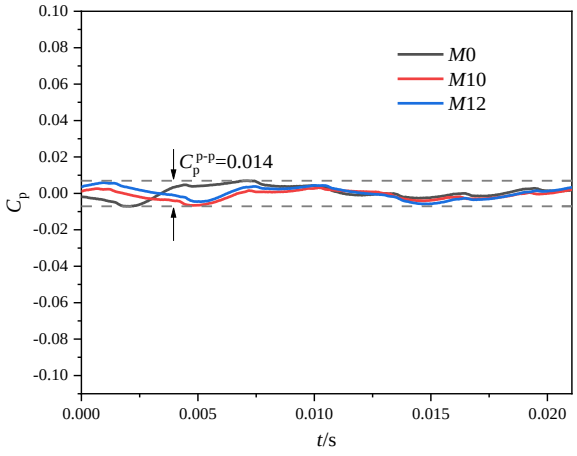

(a) Pressure coefficient of P1

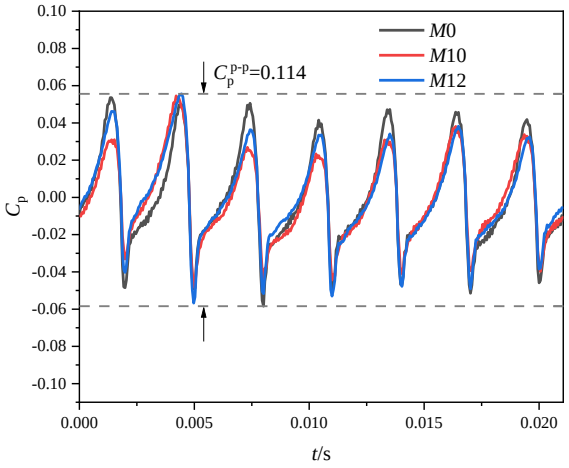

(b) Pressure coefficient of P4

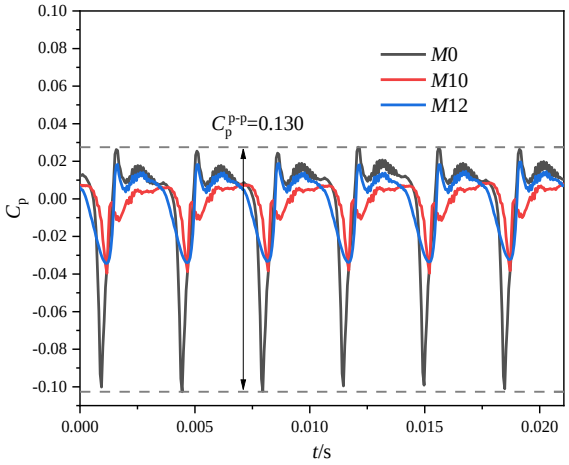

(c) Pressure coefficient of P5

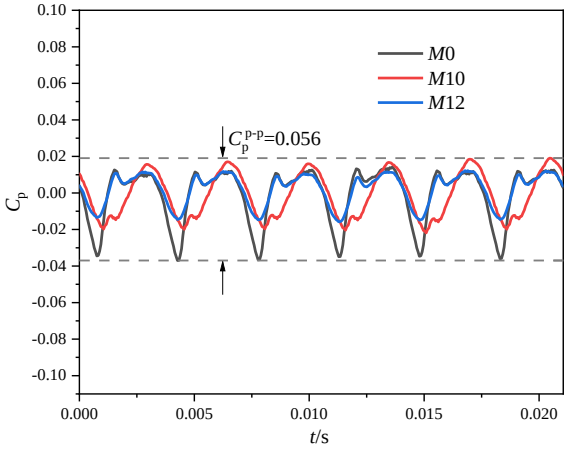

(d) Pressure coefficient of P7

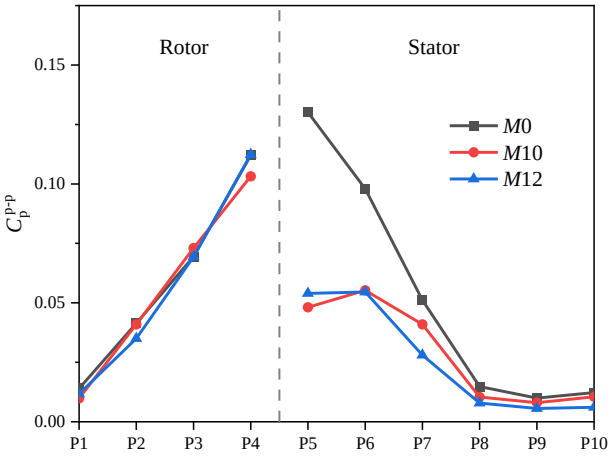

(e) Peak-to-peak pressure coefficient at each points

Fig. 18 Comparison of pressure pulsation for different BTE models

peak pressure coefficient C_p^{p-p} as shown in Eq. (29), representing the difference between the maximum and minimum pressure coefficient during one impeller revolution. Pressure fluctuations at the impeller inlet P1 are relatively small, with no clear periodic pattern. While at the impeller outlet P4, seven instances of periodic fluctuations occur, matching the number of blades in the diffuser. The closer to the impeller outlet, the larger the C_p^{p-p}, the stronger the pressure fluctuations. P5 experiences significant pressure pulsations due to its proximity to the impeller outlet. The C_p^{p-p} for *M*0 reaches 0.13 at this point. In comparison to *M*0, the pressure fluctuations for *M*10 and *M*12 are notably reduced, with C_p^{p-p} decreasing to 0.048 and 0.054, respectively. Downstream along the diffuser channel, the pressure fluctuations at P6, P7, and P8 gradually decrease. As they

reach the walls of the outlet chamber at P9 and P10, the pressure fluctuations are further reduced, with $C_p^{p\text{-}p}$ dropping to below 0.01. Six instances of periodic fluctuations occur in the stationary domains such as the pump cavity, diffuser, and outlet chamber, matching the number of blades in the impeller. Different BTE have minimal impact on pressure pulsations at monitoring points on the impeller. Changing the BTE has a more significant effect on pressure pulsations in the stationary domain near the impeller outlet, and has little effect on pressure pulsations in downstream areas away from the impeller outlet. Proper design of BTE can effectively reduce pressure pulsations, especially in the stator near the impeller outlet.

6. CONCLUSION

This study focuses on modifying the BTE of a centrifugal pump impeller using Bezier curves, rounded pressure side and cut suction side. The effect of various BTE designs on performance at rated flow rates is analyzed through simulation. Energy loss and entropy production theory are utilized to calculate and analyze the energy loss and entropy production power of each domain. Spearman correlation analysis is employed to investigate the correlation between energy loss and entropy production power and the interaction among different domains. The energy loss of the cavity and the efficiency of the pump are decomposed, and the effect of different BTE designs on them is analyzed. The effect of different BTE designs on the components of shaft power is examined. Finally, the effect of different BTE on pressure pulsations in centrifugal pump is analyzed. The following conclusions are drawn:

(1) Changing either the PS, SS, or both of them at the BTE significantly affects the performance of the centrifugal pump. Generally, a larger radius of the BTE results in higher head and power, while efficiency increases with the thinning of the BTE.

(2) The trends of energy loss and entropy production power in different BTE designs are similar for each domain, with entropy production power slightly lower than energy loss. The energy loss of each domain, in descending order, is $P_{loss,cav} > P_{loss,imp} > P_{loss,dif} > P_{loss,out} > P_{loss,in}$. The cavity experiences the largest energy loss due to primary flow loss, disc friction loss caused by the rotation of the outer cover of the impeller, and volumetric loss due to leakage.

(3) Analysis of the entropy production power components of the impeller and diffuser reveals that $P_{pro,W}$ is the largest in the impeller, while $P_{pro,D'}$ is the largest in the diffuser, with $P_{pro,\bar{D}}$ being the smallest in both cases. Different BTE designs have the greatest effect on $P_{pro,D'}$, followed by $P_{pro,W}$, and the least effect on $P_{pro,\bar{D}}$.

(4) There is an extremely strong positive correlation, with a correlation coefficient above 0.9, between energy loss and entropy production power of each domain. Each domain has the highest correlation with adjacent domains, weakening with distance. Modifying the BTE of the impeller affects not only the impeller but also downstream components like the cavity, diffuser, and outlet chamber, with minimal impact on the upstream inlet chamber.

(5) Hydraulic loss (P_h) is the largest, followed by hydraulic loss (P_v), with disc friction loss (P_m) being the smallest. Different BTE designs have the greatest effect on P_h, followed by P_v, with minimal effect on P_m. This results in mechanical efficiency (η_m) being the highest, followed by volumetric efficiency (η_v), and hydraulic efficiency (η_h) being the lowest but most affected.

(6) Shaft power is divided into five parts in descending order: Blades > Hub_o > Hub_i > Shroud_o > Shroud_i. The shaft power of blades is predominantly composed of static pressure, with $M0$, for example, reaching 88.69%. The influence of different BTE designs on shaft power primarily manifests as a static pressure load on the blades.

(7) Different BTE have the greatest influence on pressure pulsations in the stator near the impeller outlet, and reasonable design of BTE can effectively reduce pressure pulsations.

ACKNOWLEDGMENTS

This work was supported by the National Natural Science Foundation of China (Grant Nos. 52209113, 52079058), Natural Science Foundation of Jiangsu Province (Grant No. BK20220544 and BK20230011), and China Postdoctoral Science Foundation (Grant No. 2023M731367).

AUTHORS' CONTRIBUTIONS

H. Li: Conceptualization, soft-ware, formal analysis, writing—original draft preparation; **Y. Chen**: methodology, formal analysis, resources, data curation; **L. Bai**: validation, investigation, visualization; **W. Shi:** validation, visualization, supervision; **L. Zhou**: writing—review and editing, supervision, project administration, funding acquisition. All authors have read and agreed to the published version of the manuscript.

CONFLICT OF INTEREST

The authors have declared that no competing interests exist.

REFERENCES

Abramian, M., & Howard, J. (1994). Experimental investigation of the steady and unsteady relative flow in a model centrifugal impeller passage. *ASME Journal of Turbomachinery, 116*(2), 269-279. https://doi.org/10.1115/1.2928361

Al-Qutub, A. M., Khalifa, A. E., & Al-Sulaiman, F. A. (2012). Exploring the Effect of V-Shaped cut at blade exit of a double volute centrifugal pump. *Journal of*

Pressure Vessel Technology, *134*(2). https://doi.org/10.1115/1.4004798

Bourgoyne, D. A., Ceccio, S. L., & Dowling, D. R. (2005). Vortex shedding from a hydrofoil at high Reynolds number. *Journal of Fluid Mechanics*, *531*, 293-324. https://doi.org/10.1017/s0022112005004076

Cui, B., Li, W., & Zhang, C. (2020a). Effect of blade trailing edge cutting angle on unstable flow and vibration in a centrifugal pump. *Journal of Fluids Engineering-Transactions of the Asme*, *142*(10), 101203. https://doi.org/10.1115/1.4047363

Cui, B., Zhang, C., Zhang, Y., & Zhu, Z. (2020b). Influence of cutting angle of blade trailing edge on unsteady flow in a centrifugal pump under off-design conditions. *Applied Sciences*, *10*(2). https://doi.org/10.3390/app10020580

Do, T., Chen, L., & Tu, J. (2010). Numerical study of turbulent trailing-edge flows with base cavity effects using URANS. *Journal of Fluids and Structures*, *26*(7-8), 1155-1173. https://doi.org/10.1016/j.jfluidstructs.2010.07.006

El-Emam, M. A., Zhou, L., Yasser, E., Bai, L., & Shi, W. (2022). Computational methods of erosion wear in centrifugal pump: a state-of-the-art review. *Archives of Computational Methods in Engineering*, *29*(6), 3789-3814. https://doi.org/10.1007/s11831-022-09714-x

Farge, T. Z., Johnson, M. W. J. I. J. O. H., & Flow, F. (1992). Effect of flow rate on loss mechanisms in a backswept centrifugal impeller. *International Journal of Heat Fluid Flow, 13*(2), 189-196. https://doi.org/10.1016/0142-727X(92)90027-7

Gao, B., Zhang, N., Li, Z., Ni, D., & Yang, M. (2016). Influence of the blade trailing edge profile on the performance and unsteady pressure pulsations in a low specific speed centrifugal pump. *Journal of Fluids Engineering*, *138*(5). https://doi.org/10.1115/1.4031911

Gülich, J. F. (2020). *Centrifugal pumps* (4 ed.). Springer Cham. https://doi.org/10.1007/978-3-030-14788-4

Han, Y., Zhou, L., Bai, L., Shi, W., & Agarwal, R. J. P. O. F. (2021). Comparison and validation of various turbulence models for U-bend flow with a magnetic resonance velocimetry experiment. *Physics of Fluids*, *33*(12), 125117. https://doi.org/10.1063/5.0073910

Herwig, H., & Kock, F. (2006). Direct and indirect methods of calculating entropy generation rates in turbulent convective heat transfer problems. *Heat and Mass Transfer*, *43*(3), 207-215. https://doi.org/10.1007/s00231-006-0086-x

Huang, B., Zeng, G., Qian, B., Wu, P., Shi, P., & Qian, D. (2021). Pressure fluctuation reduction of a centrifugal pump by blade trailing edge modification. *Processes*, *9*(8). https://doi.org/10.3390/pr9081408

Ji, L., Li, W., Shi, W., Tian, F., & Agarwal, R. (2020). Diagnosis of internal energy characteristics of mixed-flow pump within stall region based on entropy production analysis model. *International Communications in Heat and Mass Transfer*, *117*. https://doi.org/10.1016/j.icheatmasstransfer.2020.104784

Ji, L., Li, W., Shi, W., Tian, F., & Agarwal, R. (2021). Effect of blade thickness on rotating stall of mixed-flow pump using entropy generation analysis. *Energy*, *236*. https://doi.org/10.1016/j.energy.2021.121381

Keller, J., Blanco, E., Barrio, R., & Parrondo, J. (2014). PIV measurements of the unsteady flow structures in a volute centrifugal pump at a high flow rate. *Experiments in Fluids*, *55*(10). https://doi.org/10.1007/s00348-014-1820-7

Kikuyama, K., Murakami, M., Asakura, E., Osuka, I., & Liu, J. (1985). Velocity distributions in the impeller passages of centrifugal pumps-effects of outlet edge shape of the impeller blades on the pump performance. *Bulletin of JSME*, *28*, 1963-1969. https://doi.org/10.1299/jsme1958.28.1963

Kock, F., & Herwig, H. (2004). Local entropy production in turbulent shear flows: a high-Reynolds number model with wall functions. *International Journal of Heat and Mass Transfer*, *47*(10-11), 2205-2215. https://doi.org/10.1016/j.ijheatmasstransfer.2003.11.025

Kock, F., & Herwig, H. (2005). Entropy production calculation for turbulent shear flows and their implementation in cfd codes. *International Journal of Heat and Fluid Flow*, *26*(4), 672-680. https://doi.org/10.1016/j.ijheatfluidflow.2005.03.005

Li, D., Wang, H., Qin, Y., Han, L., Wei, X., & Qin, D. (2017). Entropy production analysis of hysteresis characteristic of a pump-turbine model. *Energy Conversion and Management*, *149*, 175-191. https://doi.org/10.1016/j.enconman.2017.07.024

Li, H., Chen, Y., Yang, Y., Wang, S., Bai, L., Zhou, L., & Engineering. (2023). CFD simulation of centrifugal pump with different impeller blade trailing edges. *Journal of Marine Science and Engineering*, *11*(2), 402. https://doi.org/10.3390/jmse11020402

Li, H., Han, Y., Shi, W., Tiganik, T., & Zhou, L. (2022). Automatic optimization of centrifugal pump based on adaptive single-objective algorithm and computational fluid dynamics. *Engineering Applications of Computational Fluid Mechanics*, *16*(1), 2221-2241. https://doi.org/10.1080/19942060.2022.2143901

Lin, Y., Li, X., Li, B., Jia, X., & Zhu, Z. (2021). Influence of impeller sinusoidal tubercle trailing-edge on pressure pulsation in a centrifugal pump at nominal flow rate. *Journal of Fluids Engineering*, *143*(9). https://doi.org/10.1115/1.4050640

Lin, Y., Li, X., Zhu, Z., Wang, X., Lin, T., & Cao, H. (2022). An energy consumption improvement method for centrifugal pump based on bionic optimization of blade trailing edge. *Energy*, *246*, 123323. https://doi.org/10.1016/j.energy.2022.123323

Litfin, O., Delgado, A., Haddad, K., Klein, H., & Asme. (2017, Jul 30-Aug 03). *Numerical and experimental investigation of trailing edge modifications of centrifugal wastewater pump impellers*. ASME Fluids Engineering Division Summer Meeting, Waikoloa, HI. https://doi.org/10.1115/FEDSM2017-69123

Mansour, M., Thévenin, D., & Parikh, T. (2020). *Influence of the shape of the impeller blade trailing edge on single and two-phase airwater flows in a centrifugal pump.* Proceedings of the 36th International Pump Users Symposium. https://hdl.handle.net/1969.1/196803

Meng, C., Jiang, X. S., Wang, J., & Wei, X. M. (2019). *The complex network model for industrial data based on Spearman correlation coefficient.* 2019 International Conference on Internet of Things (Ithings) and Ieee Green Computing and Communications (Greencom) and Ieee Cyber, Physical and Social Computing (Cpscom) and Ieee Smart Data (Smartdata). https://doi.org/10.1109/iThings/GreenCom/CPSCom/SmartData.2019.00028

Mosallem, M. M. (2008). Numerical and experimental investigation of beveled trailing edge flow fields. *Journal of Hydrodynamics*, *20*(3), 273-279. https://doi.org/10.1016/S1001-6058(08)60057-8

Qian, B., Wu, P., Huang, B., Zhang, K., Li, S., & Wu, D. (2020). Optimization of a centrifugal impeller on blade thickness distribution to reduce hydro-induced vibration. *Journal of Fluids Engineering*, *142*(2). https://doi.org/10.1115/1.4044965

Wang, C., Shi, W., Wang, X., Jiang, X., Yang, Y., Li, W., & Zhou, L. (2017). Optimal design of multistage centrifugal pump based on the combined energy loss model and computational fluid dynamics. *Applied Energy*, *187*, 10-26. https://doi.org/10.1016/j.apenergy.2016.11.046

Wang, K., Ju, Y., & Zhang, C. (2019). A Quantitative evaluation method for impeller-volute tongue interaction and application to squirrel cage fan with bionic volute tongue. *Journal of Fluids Engineering*, *141*(8). https://doi.org/10.1115/1.4042372

Wu, C., Li, Q., Zheng, F., Wu, P., Yang, S., Ye, H., Huang, B., & Wu, D. (2021a). Improve of unsteady pressure pulsation based on jet–wake suppression for a low specific centrifugal pump. *Journal of Fluids Engineering*, *143*(11). https://doi.org/10.1115/1.4051402

Wu, C., Pu, K., Li, C., Wu, P., Huang, B., & Wu, D. (2022). Blade redesign based on secondary flow suppression to improve energy efficiency of a centrifugal pump. *Energy*, *246*. https://doi.org/10.1016/j.energy.2022.123394

Wu, C., Zhang, W., Wu, P., Yi, J., Ye, H., Huang, B., & Wu, D. (2021b). Effects of blade pressure side modification on unsteady pressure pulsation and flow structures in a centrifugal pump. *Journal of Fluids Engineering*, *143*(11). https://doi.org/10.1115/1.4051404

Wu, D., Yan, P., Chen, X., Wu, P., & Yang, S. (2015). Effect of Trailing-edge modification of a mixed-flow pump. *Journal of Fluids Engineering*, *137*(10). https://doi.org/10.1115/1.4030488

Zhang, F., Appiah, D., Hong, F., Zhang, J., Yuan, S., Adu-Poku, K. A., & Wei, X. (2020). Energy loss evaluation in a side channel pump under different wrapping angles using entropy production method. *International Communications in Heat and Mass Transfer*, *113*. https://doi.org/10.1016/j.icheatmasstransfer.2020.104526

Zhang, N., Liu, X., Gao, B., Wang, X., & Xia, B. (2019). Effects of modifying the blade trailing edge profile on unsteady pressure pulsations and flow structures in a centrifugal pump. *International Journal of Heat and Fluid Flow*, *75*, 227-238. https://doi.org/10.1016/j.ijheatfluidflow.2019.01.009

Zhao Z, Zhou L, Bai L, Wang B & Agarwal R. (2024) Recent advances and perspectives of CFD–DEM simulation in fluidized bed. *Archives of Computational Methods in Engineering, 31*, 871-918. https://doi.org/10.1007/s11831-023-10001-6

Zhou, L., Hang, J., Bai, L., Krzemianowski, Z., El-Emam, M. A., Yasser, E., & Agarwal, R. (2022). Application of entropy production theory for energy losses and other investigation in pumps and turbines: A review. *Applied Energy*, *318*. https://doi.org/10.1016/j.apenergy.2022.119211

Zobeiri, A., Ausoni, P., Avellan, F., & Farhat, M. (2012). How oblique trailing edge of a hydrofoil reduces the vortex-induced vibration. *Journal of Fluids and Structures*, *32*, 78-89. https://doi.org/10.1016/j.jfluidstructs.2011.12.003